Author's personal copy

Icarus 221 (2012) 135–146

Contents lists available at SciVerse ScienceDirect

Icarus

journal homepage: www.elsevier.com/locate/icarus

The effect of surface topography on the lunar photoelectron sheath and electrostatic dust transport

Andrew R. Poppe [a,e,*], Marcus Piquette [b], Alexandre Likhanskii [c], Mihály Horányi [b,d,e]

[a] Space Sciences Laboratory, 7 Gauss Way, University of California at Berkeley, Berkeley, CA 94720, USA
[b] Colorado Center for Lunar Dust and Atmospheric Studies, Laboratory for Atmospheric and Space Physics, University of Colorado, UCB 392, Boulder, CO 80303, USA
[c] Tech-X Corporation, 5621 Arapahoe Ave., Suite A, Boulder, CO 80303, USA
[d] Department of Physics, University of Colorado, Boulder, CO 80309, USA
[e] NASA Lunar Science Institute, Mountain View, CA 94089, USA

ARTICLE INFO

Article history:
Received 7 May 2012
Revised 19 July 2012
Accepted 22 July 2012
Available online 1 August 2012

Keywords:
Moon, Surface
Asteroids, Surface
Regoliths

ABSTRACT

The dayside near-surface lunar plasma environment is electrostatically complex, due to the interaction between solar UV-induced photoemission, the collection of ambient ions and electrons, and the presence of micron and sub-micron sized dust grains. Further complicating this environment, although less well understood in effect, is the presence of surface relief, typically in the form of craters and/or boulders. It has been suggested that such non-trivial surface topography can lead to complex electrostatic potentials and fields, including "mini-wakes" behind small obstacles to the solar wind flow and "supercharging" near sunlit-shadowed boundaries (Criswell, D.R., De, B.R. [1977]. J. Geophys. Res. 82 (7); De, B.R., Criswell, D.R. [1977]. J. Geophys. Res. 82 (7); Farrell, W.M., Stubbs, T.J., Vondrak, R.R., Delory, G.T., Halekas, J.S. [2007]. Geophys. Res. Lett. 34; Wang, X., Horányi, M., Sternovsky, Z., Robertson, S., Morfill, G.E. [2007]. Geophys. Res. Lett. 34, L16104). In this paper, we present results from a three-dimensional, self-consistent, electrostatic particle-in-cell code used to model the dayside near-surface lunar plasma environment over a variety of local times with the presence of a crater. Additionally, we use the particle-in-cell model output to study the effect of surface topography on the dynamics of electrostatic dust transport, with the goal of understanding previous observations of dust dynamics on the Moon and dust ponding on various asteroids.

© 2012 Elsevier Inc. All rights reserved.

1. Introduction

As an airless body with no global magnetic field, the Moon is exposed to both solar ultraviolet (UV) radiation and ambient electrons and ions. On the dayside for small solar zenith angles (SZAs), the photoemission current is typically larger than the ambient plasma collection current by at least an order of magnitude (Feuerbacher et al., 1972) and a photoelectron sheath develops above the surface (Guernsey and Fu, 1970; Fu, 1971; Nitter et al., 1998; Poppe and Horányi, 2010). Previous simulations of the lunar photoelectron sheath in the solar wind using a one-dimensional particle-in-cell (PIC) code have determined typical potentials of +5 V, electric field strengths of ≈5 V/m and sheath thicknesses of 1 m near the sub-solar point (Poppe and Horányi, 2010). As the SZA is increased, the sheath is expected to become progressively weaker, before transitioning to a negative plasma sheath near the lunar terminator (Farrell et al., 2007; Halekas et al., 2008).

The presence of both craters and boulders may lead to a variety of complex plasma environments on the lunar surface due to UV and ambient plasma shadowing, including the generation of "mini-wakes", characterized by local losses of quasineutrality and associated ambipolar electric fields (De and Criswell, 1977; Criswell et al., 1977; Farrell et al., 2007, 2008, 2010; Zimmerman et al., 2011). The typical Debye length on the dayside lunar surface is roughly 1 m, which implies that topographical structures larger than this scale should not significantly affect the lunar near-surface plasma environment; however, this may be overly simplistic in that the extremely low conductivity of the Moon may allow for the generation of strong local electric fields due to differential surface charging near sunlit-shadowed boundaries (Olhoeft et al., 1974; Criswell et al., 1977; De and Criswell, 1977; Wang et al., 2007). While in the solar wind, the Moon is continually bathed in a 10 eV electron plasma with a Debye length of roughly 10 m, which will tend to short out electric fields over distances larger than this. The maximum strength to which electric fields on the lunar surface can grow in the simultaneous presence of photoelectrons, ambient solar wind plasma, and differential surface shadowing is currently an open question.

* Corresponding author at: Space Sciences Laboratory, 7 Gauss Way, University of California at Berkeley, Berkeley, CA 94720, USA.
E-mail address: poppe@ssl.berkeley.edu (A.R. Poppe).

0019-1035/$ - see front matter © 2012 Elsevier Inc. All rights reserved.
http://dx.doi.org/10.1016/j.icarus.2012.07.018

Author's personal copy

Complex electric fields above the surfaces of airless bodies are of geophysical interest in that they have been hypothesized as a method for amplifying electrostatic dust transport. At the Moon, several observations of increased electrostatic dust dynamics near the terminator, including of the detection of slowly-moving, highly charged dust grains by the Apollo 17 Lunar Ejecta and Meteorites Experiment (Berg et al., 1973, 1974), images of lunar horizon glow near the terminator by the Surveyor 5, 6 and 7 spacecraft (Criswell, 1972; Rennilson and Criswell, 1974; Pelizzari and Criswell, 1978), and the presence of excess brightness in several Apollo coronagraph images (McCoy and Criswell, 1974; Glenar et al., 2011) have suggested that spatially complex electric fields may contribute to elevated dust grain charging and acceleration. Observations from the NEAR spacecraft around the Asteroid 433 Eros have shown the presence of 'dust ponds' in the center of several craters. One hypothesis for their formation is the accumulation of micron-sized dust grains within craters via electrostatic transport (Robinson et al., 2001; Veverka et al., 2001; Cheng et al., 2002). Mercury, as an airless body, has also been suggested to contain the requisite environment for electrostatic dust transport (Ip, 1986).

Previous modeling efforts have explored the possibility of electrostatic dust transport above the surfaces of airless bodies, mainly via a combination of a plasma model (usually determined either from theoretical equations or plasma modeling) and test-particle dust tracing (Lee, 1996; Nitter et al., 1998; Colwell et al., 2005; Borisov and Mall, 2006; Hughes et al., 2008; Poppe and Horányi, 2010). Over time, these models have become progressively more complex and realistic in their description of both the plasma environment around airless bodies and their treatment of dust grain motion; however, open questions still remain, including the role of both topography, such as craters or boulders, and varying solar zenith angle in modifying the near-surface plasma environment, the influence that complex electric fields near craters and boulders have on the electrostatic transport of dust grains, and the ability of craters to accumulate dust grains via electrostatic transport over long periods of time. Laboratory work has confirmed some aspects of the theory of electrostatic dust transport, including the ability to charge and levitate dust grains in a plasma sheath (Sickafoose et al., 2001, 2002; Robertson et al., 2003; Flanagan and Goree, 2006; Wang et al., 2009), the presence of elevated electric fields near differentially charged surfaces (Wang et al., 2007), and the electrostatic transport of dust grains near an electron beam impact/shadow boundary (Wang et al., 2010, 2011).

In this paper, we present a series of three-dimensional, electrostatic particle-in-cell (PIC) simulations of the lunar photoelectron sheath in the presence of a surface crater and use the modeled plasma environment to simulate electrostatic dust transport via a test-particle approach. We describe the particle-in-cell model and present results from the simulations in Section 2. In Section 3, we describe our test-particle approach to modeling electrostatic dust transport and present results from the model, including the typical behavior of an individual grain and the net transport of a spatial distribution of dust grains. Finally, we discuss the implication of our results for dust transport at airless bodies and conclude in Section 4.

2. Particle-in-cell simulations

2.1. Model description

We have modeled the three-dimensional dayside near-surface lunar plasma environment at a variety of solar zenith angles (SZAs) with the presence of an approximately 7 m diameter, 1 m deep crater. The simulations were performed by VORPAL, a relativistic, arbitrary dimensional plasma simulation code, run in PIC mode (the code is capable of modeling in either fluid or PIC mode) (Nieter and Cary, 2004). The simulation domain consisted of a $150 \times 150 \times 150$ grid with uniform spacing equal to 0.1 m, smaller than the local Debye length. The time step for the simulations was set to 20 ns in order to accurately resolve charged particle dynamics and, in particular, the electron energy distribution function. Poisson's equation was solved in three dimensions for the electrostatic potential and electric field distributions using a biconjugate gradient stabilized method with multigrid preconditioner from the Trilinos mathematical algorithm package (Heroux et al., 2005). The tolerance for the convergence was chosen to be 10^{-8}. The region 0.1 m under the crater surface was kept at zero potential while Neumann boundary conditions with zero normal electric field were applied to the rest of the simulation domain boundaries. Charged particles were represented as macroparticles (collection of charged particles with identical properties) with each macroparticle consisting of 10^5 physical particles. Such an approach allowed us to significantly reduce the simulation time without loss of accuracy.

The solar wind is injected at the top and the sides of the simulation volume, with a bulk flow speed of 450 km/s, density of approximately $10^7\ m^{-3}$, and 10 eV Maxwellian ion and electron distributions. Photoelectrons are emitted from the surface with a 2.2 eV Maxwellian distribution and a sub-solar photocurrent of $J_{ph} = 4.5 \times 10^{-6}\ \mu A\ m^{-2}$ (Feuerbacher et al., 1972). The photocurrent at any point on the surface scales as $\cos\theta$, where θ is the angle between solar incidence and the local surface normal. The model also includes the effect of shadowing in the photoemission of electrons for regions that are shadowed by the crater rim at larger solar zenith angles. The lunar surface is modeled as an insulator, with surface charge calculated by keeping track of emitted and absorbed photoelectrons as well as any absorbed solar wind ions and electrons. Thus, areas in sunlight will tend to charge positively due to the larger photoemission current, while areas in shadow will charge negatively, due to the combined charging from the collection of solar wind electrons and ambient photoelectrons. VORPAL periodically reports out the particle positions for all species (solar wind ions, solar wind electrons, photoelectrons, surface charge), the electrostatic potential, and the electric field for the entire simulation volume. All simulations are allowed to come to equilibrium before using any data for analysis.

The topography we selected to model in this first study is intended to investigate the combined effect of the variation in solar zenith angle and the presence of moderate-scale surface relief. The crater size, at approximately 7 m in diameter, was chosen to be simultaneously larger than the near-surface Debye length of approximately 1 m (given typical photoelectron densities at the sub-solar point of $10^8\ m^{-3}$), while smaller than the maximum simulation length attainable given our computational constraints. Surface relief at scales greater than or equal to the near-surface Debye length are not expected to influence the plasma equilibrium given that a plasma will tend to short out electric fields on Debye-length scales. We placed the crater along the equatorial plane and varied the solar zenith angle over a series of angles from 0° to 90° in 15° intervals. Since the crater is symmetric with respect to the sub-solar point, this range of solar zenith angles provides a full day (dawn to dusk).

2.2. Model results

Fig. 1 shows the electrostatic potential referenced to the mean value of the potential at a height of 15 m above the lunar surface as a function of height and lateral distance above the crater through the plane containing the surface normal (far from the crater) and the solar incidence vector, through the center of the crater, for 0° solar zenith angle. The lunar surface is denoted as a black

Author's personal copy

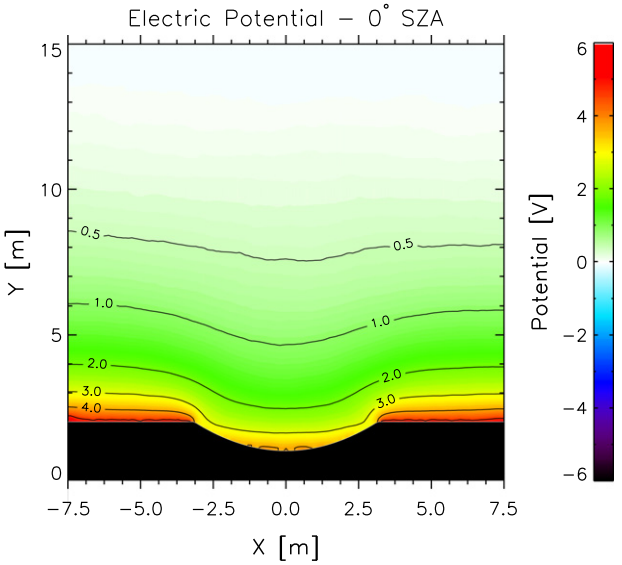

Fig. 1. The electric potential above the surface of the Moon with a 7 m-diameter crater present for 0° solar zenith angle (noon). Photoemission and the solar wind are both included in these simulations. The lines mark individual potential contours in Volts for interpretation.

shaded region with the crater extending from approximately −3.5 m to 3.5 m. For this case, a typical photoelectron sheath forms at the lunar surface away from the crater, with maximum surface potentials with respect to infinity of approximately +5 V. Within the crater, the photoelectron sheath is weaker, as the sloping floor of the crater emits less photocurrent and therefore, charges less. The effect of the crater on the equipotential contours can be readily seen in Fig. 1, in that a depression in the electrostatic potential appears just above the crater. Part of this effect is because the crater surface is at a lower height than the surrounding flat surface and part is due to the decreased photoemission from inside the crater. Combined together, these factors cause the equipotential contours to drop more than a meter in height directly above the crater.

Fig. 2 shows the electrostatic potential for solar zenith angles ranging from 0° to 75° in the same plane as presented in Fig. 1 zoomed into the region just around and above the crater. In each panel, an arrow on the right-hand side denotes the direction of incoming solar UV radiation and solar wind. As the solar zenith angle transitions from 0° to 30°, shown in panels Fig. 2a–c, two main changes occur. Outside the crater, the photoelectron sheath begins to weaken, down to a surface potential with respect to infinity of approximately +4 V. Inside the crater, the electrostatic potential takes on a more complicated morphology, as the point of maximum illumination (the point where the surface normal is parallel to the incoming solar UV radiation vector) moves farther towards the left rim of the crater. The surface potential within the crater is maximum at the point of maximum illumination, while the potential begins to progressively decrease on the opposite side of the crater. At 30° solar zenith angle, the potential on the sunward side of the crater has dropped to less than +2 V, as photoemission is decreased from this area and collection of ambient photoelectrons from the stronger emitting portions of the surface increases.

Once the solar zenith angle has reached 45°, shown in Fig. 2d, a small portion of the sunward side of the crater (between approximately 2.5 and 3.25 m) is shadowed by the right lip of the crater. Correspondingly, the electrostatic potential just above this part of the crater surface falls to zero, shaded white in Fig. 2d. Additionally, the sheath potential outside of the crater continues the decreasing trend seen from 0° to 30° SZA. At 60°, shown in Fig. 2e, the shadowing of the sunward portion of the crater increases and both of these trends continue. Notably, the sunward side of the crater reaches a negative potential of approximately −2 V, indicating that this part of the lunar surface is charged negatively. Since this region of negative surface charge is adjacent to regions of positive surface charge on both sides (on the opposite side of the crater and outside of the crater on the sunward side), significant horizontal electric fields will appear, especially near the crater lip (x = +3.5 m), where the transition from negative to positive surface charge occurs over an extremely short distance (<0.1 m). Finally at 75°, shown in Fig. 2f, the electrostatic potential throughout the volume has a magnitude of <2 V, and displays a dipolar-like structure within the crater, as nearly half of the surface inside the crater is shadowed.

Fig. 3 shows the individual electric field components and the total electric field magnitude along the lunar surface for three solar zenith angles: (a) 15°, (b) 45°, and (c) 75°. For (a) 15°, the Sun is nearly overhead and the electric field outside of the crater is mainly vertical and approximately 3–5 V/m, consistent with previous simulations (Poppe and Horányi, 2010). Inside the crater, the electric field is significantly smaller at <2 V/m, although still mainly vertical. The horizontal component of the electric field is slightly positive (<1 V/m) on the left side of the crater and transitions smoothly to slightly negative near the opposite side. Near the crater edges, however, both the vertical and horizontal electric field components increase significantly. On the left edge of the crater, both components reach a maximum of approximately +5 V/m, for a total electric field strength of approximately 7 V/m. On the opposite (right) side of the crater, both components show similar strength maxima, with the horizontal electric field component pointing in the opposite direction.

In Fig. 3b, we see that the electric field outside of the crater, while still being mainly in the vertical direction, is weaker than at 15° SZA, as expected from the decreased photoemission current. Inside the crater, the electric field is roughly constant at strengths similar to 15°, however, the individual components behave differently. The vertical electric field component is positive for most of the crater interior and transitions to negative values (downward-pointing) near the right edge. In concert with this, the horizontal component is slightly positive through most of the crater (in contrast to the 15° case where is approaches zero near the crater center), and increases slightly near x = +2 m before becoming negative at the crater edge. The electric field at the left crater edge does not show a spike, in contrast to the 15° case, while the right crater edge shows a similarly strong spike. The absence of an electric field spike at the left edge is due to the smooth transition in surface charge (and hence, potential) across the left edge of the crater.

Finally, Fig. 3c, at 75° SZA, shows a significant reduction in electric field strength across the entire surface, both within and outside of the crater, as the Sun and solar wind flux strike the surface at a large incidence angle. Outside the crater, the field is still mainly vertical, albeit at magnitudes of less than 1 V/m. Inside the crater, the magnitude is similar, although mainly positively horizontal, with a vertical component that transitions from positive on the left, slightly sunlit side of the crater, to negative, on the shadowed edge of the crater. Additionally, the electric field shows spikes at both crater edges, although, the magnitude of both spikes is at most approximately 3 V/m, much less than in either the 15° or 45° cases. The decreased photoemission at such a large solar zenith angle strictly limits the strength of the near-surface photoelectric fields.

While Fig. 3 shows the variation of the electric field along the lunar surface, we also wish to explore the spatial structure of the electric fields as a function of height above the lunar surface. Fig. 4 shows the horizontal component (E_x), vertical component

Author's personal copy

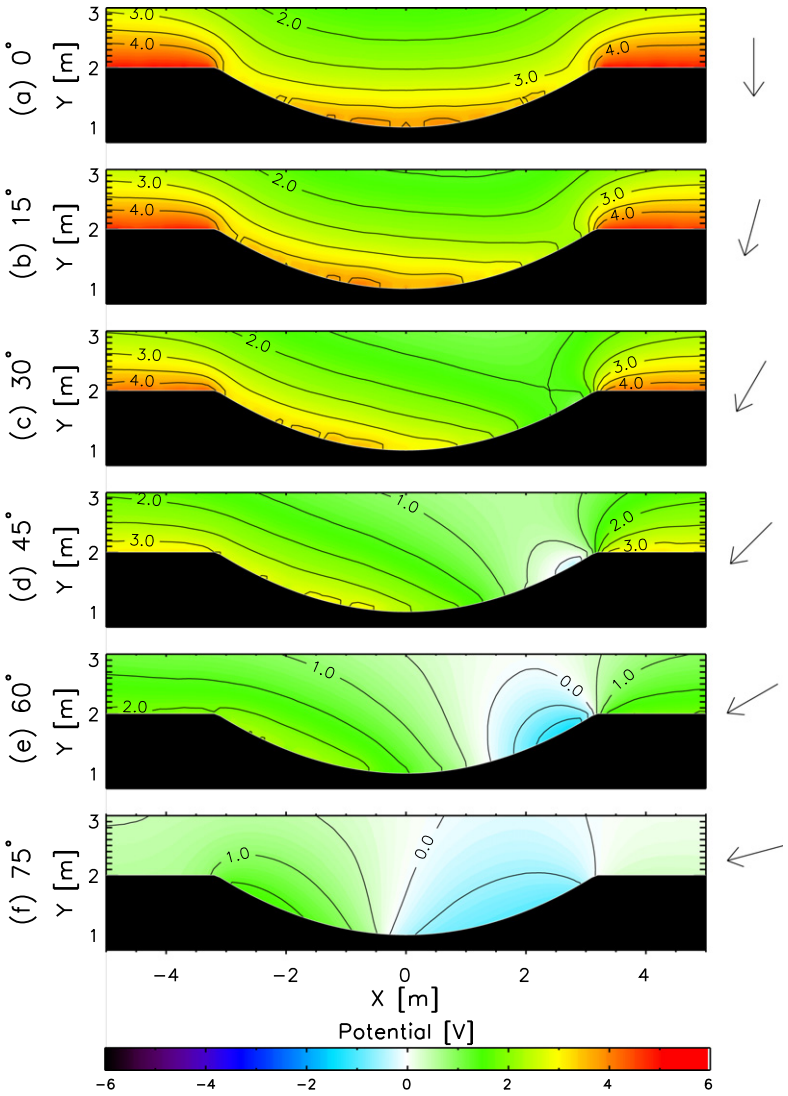

Fig. 2. The electric potential above a crater on the surface of the Moon for a series of solar zenith angles zoomed into the near-crater region for clarity. Overplotted are contour lines at 0.5 V intervals. The arrows along the right-hand side denote the incoming direction of solar UV radiation and the solar wind.

(E_y), and total magnitude of the electric field near the sunward crater edge for a solar zenith angle of 45°. The horizontal component shows two distinct regions of opposite polarity, with approximately 2 V/m fields pointing sunward inside the crater and a lobe-like region of anti-sunward pointing electric field ranging up to −7.5 V/m. The vertical component consists of roughly 2 V/m fields near the crater center ($x = 0$ m) and farther sunward than the crater edge ($x > 4$ m). Near the crater edge, however, the vertical component consists of two, strong ($|E_y| > 5$ V/m) oppositely directed regions immediately bounding the edge. Just inside the crater, the vertical component of the electric field points down into the negatively-charged crater wall, while just outside the crater, the vertical component is enhanced in the upward direction over its nominal strength far from the crater. The total magnitude of the electric field, shown in Fig. 4c, shows a marked increase in the electric field strength within approximately 0.5 m centered on the crater edge over the electric field strength far from the crater. The combination of relatively simple crater topography and non-zero solar zenith angle gives rise to a nearly threefold increase in the electric field strength.

Fig. 5 shows the maximum electric field magnitude within or near the crater (defined as within 1 m of the crater edge) and the mean electric field far from the crater as a function of solar zenith angle. The mean fields far from the crater provide a control case with which to compare the electric field enhancement induced by the presence of the crater. The maximum mean strength occurs at a solar zenith angle of zero degrees at approximately 5 V/m, as expected from previous work (Poppe and Horányi, 2010). As the SZA increases to approximately 60°, the mean electric field magnitude decreases to roughly 1 V/m. A sharp drop occurs at 75°, near the point at which the sheath transitions from a positive photoelectron-dominated sheath to a negative, solar wind electron sheath, in agreement with previous work (Farrell et al., 2007). For a solar zenith angle of 90° (not shown in Fig. 1), the magnitude of the electric field far from the crater increases, as the last remanent of photoemission is extinguished and the solar wind electron collection current dominates the lunar sheath. Note that while the magnitude increases at 90°, the electric field direction is in fact negative (pointing towards the surface) for this case. The maximum electric field strength in the crater follows a roughly similar profile to the mean electric field strength far from the crater as a function of solar zenith angle, with a two- to threefold increase in magnitude. Within the crater, maximum electric fields on the order of 10 V/m persist throughout most of the lunar day, before

Author's personal copy

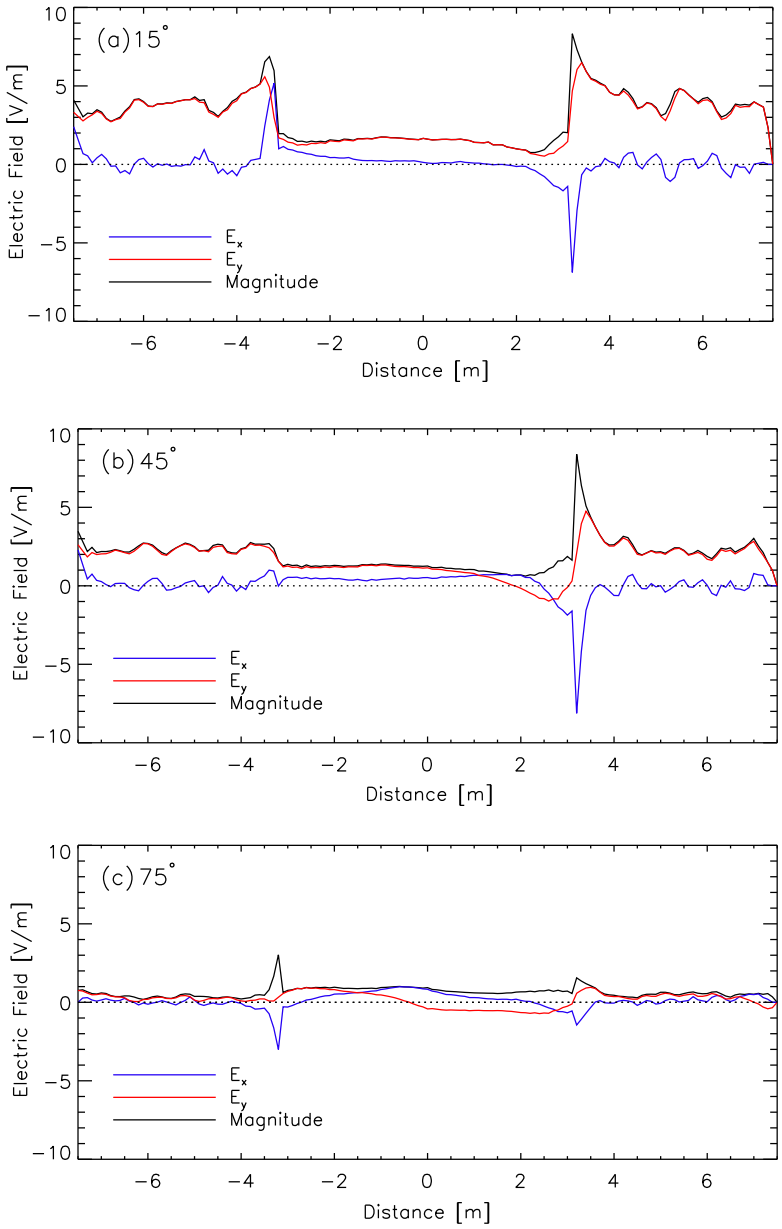

Fig. 3. The electric field (E_x, E_y components and the total magnitude) along the lunar surface for three cases of solar zenith angle: (a) 15°, (b) 45°, and (c) 75°, taken from the simulations presented in Fig. 2b, d, and f, respectively.

decreasing past solar zenith angles of 60°. At 75°, where the mean electric field far from the crater nearly vanishes, the maximum electric field strength within the crater is approximately 3 V/m, nearly that of the electric field far from the crater at noon. Finally, the maximum electric field within the crater drops further at 90°, becoming nearly equal to the electric field magnitude outside the crater.

3. Dust particle levitation

Previous work has investigated the ability of sheaths (either positively or negatively charged) to electrostatically charge, levitate, and transport micron-sized dust grains. Theoretical analyses have suggested that dust grain transport may range from levitation and horizontal transport near the lunar terminators (Borisov and Mall, 2006) to a more ballistic, single-hop like motion through most of the lunar day (Stubbs et al., 2007). Laboratory experiments, done mainly in negative sheaths, have shown a wide range of dust grain charging and transport (Sickafoose et al., 2000, 2001, 2002; Wang et al., 2009, 2010, 2011). Simulations have ranged from 1- and 3-dimensional test-particle methods with one-dimensional plasma environments taken from theoretical calculations (Colwell et al., 2005; Hughes et al., 2008), to a one-dimensional test-particle method with the plasma environment derived from a one-dimensional PIC simulation (Poppe and Horányi, 2010). Collectively, these investigations have provided significant evidence for the possibility of electrostatically-induced dust grain transport above the lunar surface; however, significant questions still remain, especially with regards to how dust transport is affected by the presence of self-consistent, three-dimensional plasma densities and electric fields. Our work presented here uses the three-dimensional PIC-derived plasma environment described in the previous section to investigate two-dimensional dust grain charging and transport in the vicinity of a lunar crater.

Author's personal copy

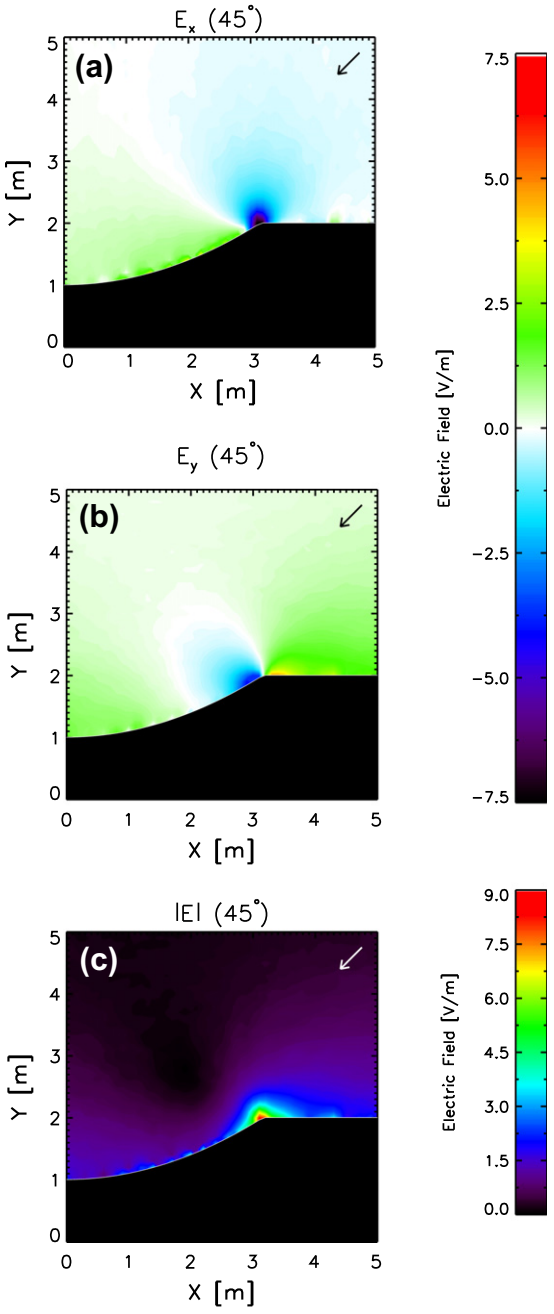

Fig. 4. The (a) horizontal component (E_x), (b) vertical component (E_y), and (c) magnitude of the electric field above one side of the crater edge for a solar zenith angle of 45°, taken from the same simulation shown in Fig. 2d. The arrow denotes the direction of solar UV radiation and the solar wind flux. Note the different color scales for the components versus the magnitude. (For interpretation of the references to color in this figure legend, the reader is referred to the web version of this article.)

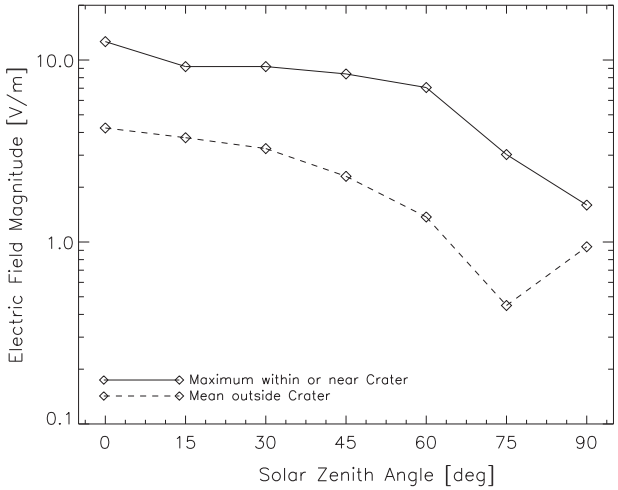

Fig. 5. The maximum electric field magnitude within or near the crater (solid line) and the mean electric field magnitude outside the crater as a function of solar zenith angle.

3.1. Model description

To model dust dynamics within the near-surface lunar plasma environment, we developed a two dimensional dust tracing code, based on earlier work where individual dust grains are introduced into a PIC-modeled plasma environment (Poppe and Horányi, 2010). Due to computational constraints, the dust grain dynamics model was run with only two dimensions by allowing dust grains to move within the two-dimensional plane containing the surface normal (away from the crater) and the solar UV/solar wind incidence vector, through the center of the crater. The model uses the same topography as shown in Fig. 1, with an approximately 7 m diameter, 1 m deep crater. Previous simulations have shown that dust grains launched from the lunar surface with velocities greater than approximately 4 m/s follow purely ballistic trajectories that are unmodified by the presence of typical photoelectron sheath electric fields, regardless of size and assuming a density of 2.5 g/cm^3 (Poppe and Horányi, 2010). Thus, for our model, the initial dust grain launch velocity was chosen to be 1 m/s. The initial charge on the dust grain was calculated using the net lunar surface charge density of $+3 \times 10^8$ e/m^2 as determined by previous PIC simulations (Poppe and Horányi, 2010). With this surface charge density, the average dust grain on the surface would have either 0 or 1 elementary positive charge. For the simulations presented here, we started all dust grains with 1 elementary positive charge. Once a dust grain is launched off the surface, it interacts with the ambient plasma and the dust grain motion is calculated by integrating the following coupled equations of motion:

$$\frac{dx}{dt} = v_x \tag{1}$$

$$\frac{dy}{dt} = v_y \tag{2}$$

$$\frac{dv_x}{dt} = \frac{qE_x(x,y)}{m_d} \tag{3}$$

$$\frac{dv_y}{dt} = \frac{qE_y(x,y)}{m_d} - g_{moon} \tag{4}$$

$$\frac{dq}{dt} = I_{ph}(q) - I_{phc}(x,y,q) - I_{swe}(x,y,q) + I_{swi}(x,y,q), \tag{5}$$

where x, v_x and E_x are the position, velocity and electric field in the x-direction, respectively, y, v_y and E_y are the position, velocity and electric field in the y-direction, respectively, q is the charge on the grain, m_d is the mass of the grain, and $g_{moon} = 1.6$ m/s^2 is the lunar gravitational acceleration. The charging currents include the photoemission current from the grain, I_{ph}, the collection of ambient photoelectrons, I_{phc}, the collection of ambient solar wind electrons, I_{swe}, and the collection of ambient solar wind ions, I_{swi}, as given by Horányi (1996).

Fig. 6 shows an example trajectory in panel (a) and the dust grain horizontal velocity, vertical velocity, local horizontal electric field, local vertical electric field, and grain charge in panels (b)–(f) for a 24 nm radius grain at a solar zenith angle of 0° (noontime). The grain was launched off the lunar surface at a position of

Author's personal copy

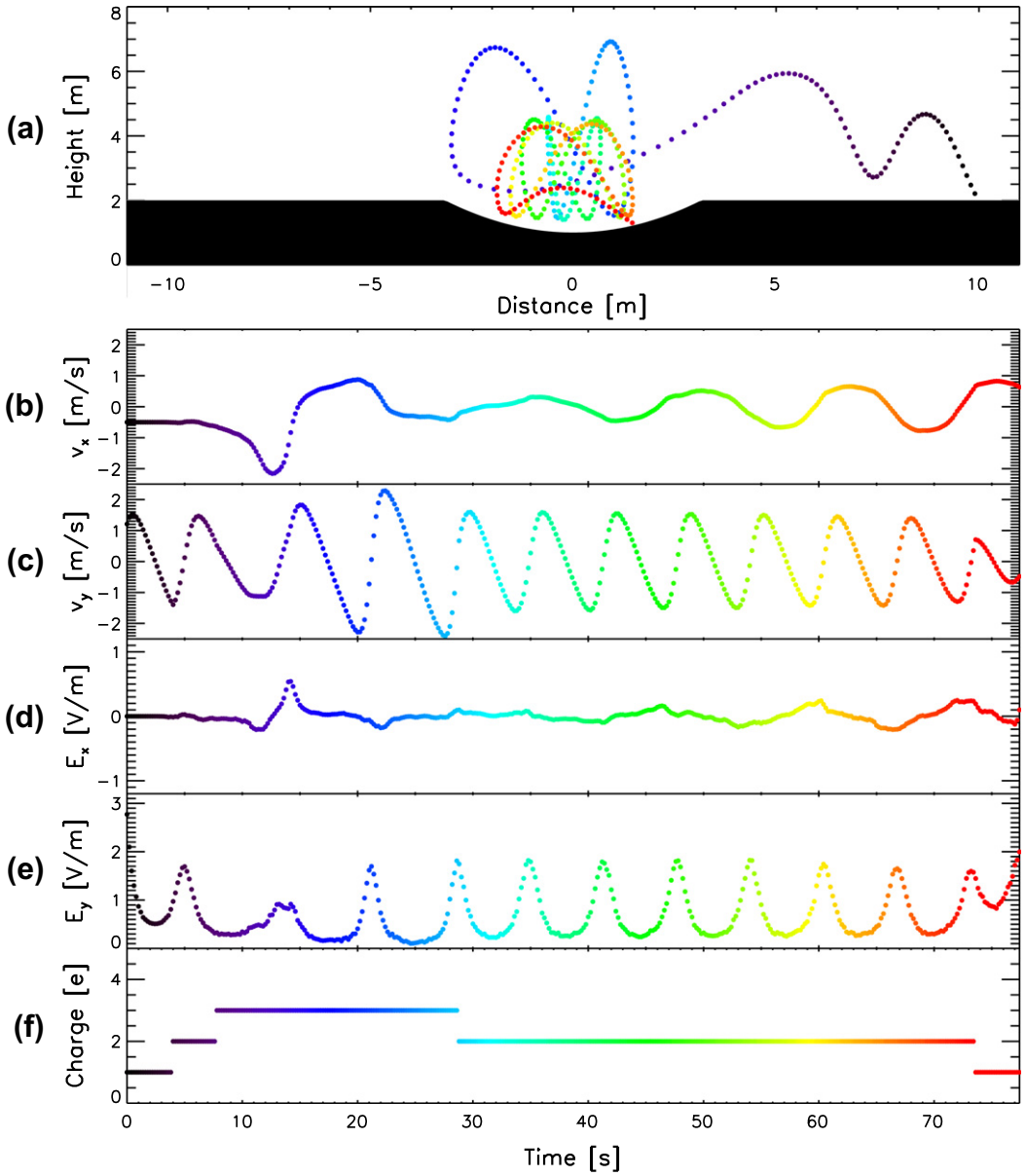

Fig. 6. A representative example of an individual lunar dust grain simulation. The top panel shows the spatial trajectory of a 24 nm dust grain above the lunar surface with a crater present. The five time series panels show the horizontal and vertical velocity, v_x and v_y, respectively, the horizontal and vertical components of the electric field, E_x and E_y, respectively, and the grain charge (in units of fundamental charges).

$x = +10$ m, with an initial velocity of 1 m/s at an angle from the surface normal of 30°. The spatial path of the trajectory, shown in panel (a), is color-coded as a function of time, and the associated variables, shown in panels (b)–(f), are colored to match. As the grain initially leaves the surface it gains two additional charges within the first 10 s. This charge allows the surface photoelectric field, positive and vertical at this horizontal distance from the crater, to electrostatically reflect the grain before it re-impacts the surface. Following this oscillation, the grain attains a slightly higher maximum height while approaching the crater. At this point ($t \approx 12$ s), the grain enters a region of slightly negative horizontal electric field. With the grain charged positively, this field accelerates the grain horizontally over the crater while gravity simultaneously accelerates the grain towards the surface. The grain approaches the left edge of the crater and is reflected both upwards and sunwards by the electric field. At this point ($t \approx 15$ s), the grain becomes essentially trapped within the region above the crater, oscillating multiple times between the left and right edges of the crater. Each time the grain approaches the surface, it is reflected both upwards and in the opposite horizontal direction. While Fig. 6c shows that the vertical velocity, v_y, enters a stable oscillatory period between approximately $t = 30$ and 75 s, panel Fig. 6b shows that the horizontal velocity, while oscillating, grows slightly over time. This growth in kinetic energy is at the expense of the particle's gravitational potential energy, as the particle's maximum height slowly decreases during this time (Fig. 6a). The overall energy of the particle (kinetic plus gravitational plus electrostatic) is conserved, with the exception of times when the grain gains or loses a charge. Eventually, the grain re-impacts the sunward wall of the crater and the simulation is halted. This example trajectory shows that individual dust grain motion within the plasma environment generated near a lunar crater can be complex due to the presence of spatially variable vertical and horizontal electric field components.

Author's personal copy

3.2. Net dust transport

As discussed earlier, several experimental, theoretical, and in situ analyses have suggested that micron and sub-micron sized dust grains can be electrostatically transported above the surfaces of airless bodies, including the Moon and asteroids. One such observation, made by the NEAR spacecraft above the Asteroid 433 Eros (Veverka et al., 2001; Robinson et al., 2001; Cheng et al., 2002), showed the presence of ponded deposits in the center of several craters on the asteroid's surface. One theory for this phenomenon is accumulation of micron and sub-micron sized grains from the local regolith into the crater interior via electrostatic transport. Previous simulations have investigated this phenomenon and found general agreement with observation (Colwell et al., 2005; Hughes et al., 2008). Here we extend that work by using a fully self-consistent, three-dimensional plasma environment in which the dust grains are embedded.

In order to simulate the net electrostatic transport of lunar dust grains, we use the series of PIC plasma simulation results presented in Section 2. To construct the plasma densities and electric fields above the lunar crater at any time during the lunar day, we use simple interpolation between the discrete SZAs we have simulated. For example, to determine the plasma environment at a solar zenith angle of 37.5°, we equally weight the densities and electric fields between the 30° and 45° PIC simulation results. Also, while our PIC simulation region extends to horizontal distances of ±7.5 m, we extend the horizontal simulation range for the dust particle transport simulation to ±25 m by using the plasma parameters (density, electric field, etc.) at the PIC simulation boundaries for the plasma environment at ±7.5 m outwards. In essence, the plasma environment is constant for horizontal distances from the crater greater than 7.5 m, while within 7.5 m (corresponding to the PIC simulation region), the plasma characteristics are given by the explicit PIC results.

We begin the dust transport simulation at dawn (SZA = 90°) by distributing 25,000 dust grains with sizes randomly chosen between 10 nm and 10 μm, evenly distributed across the surface (both within and outside of the crater). As time progresses from dawn, the plasma environment is continuously updated and dust grains are launched at a rate of one grain per second with an initial velocity of 1 m/s at a random angle from the surface normal between 0° and 45°. The model boundary conditions for dust

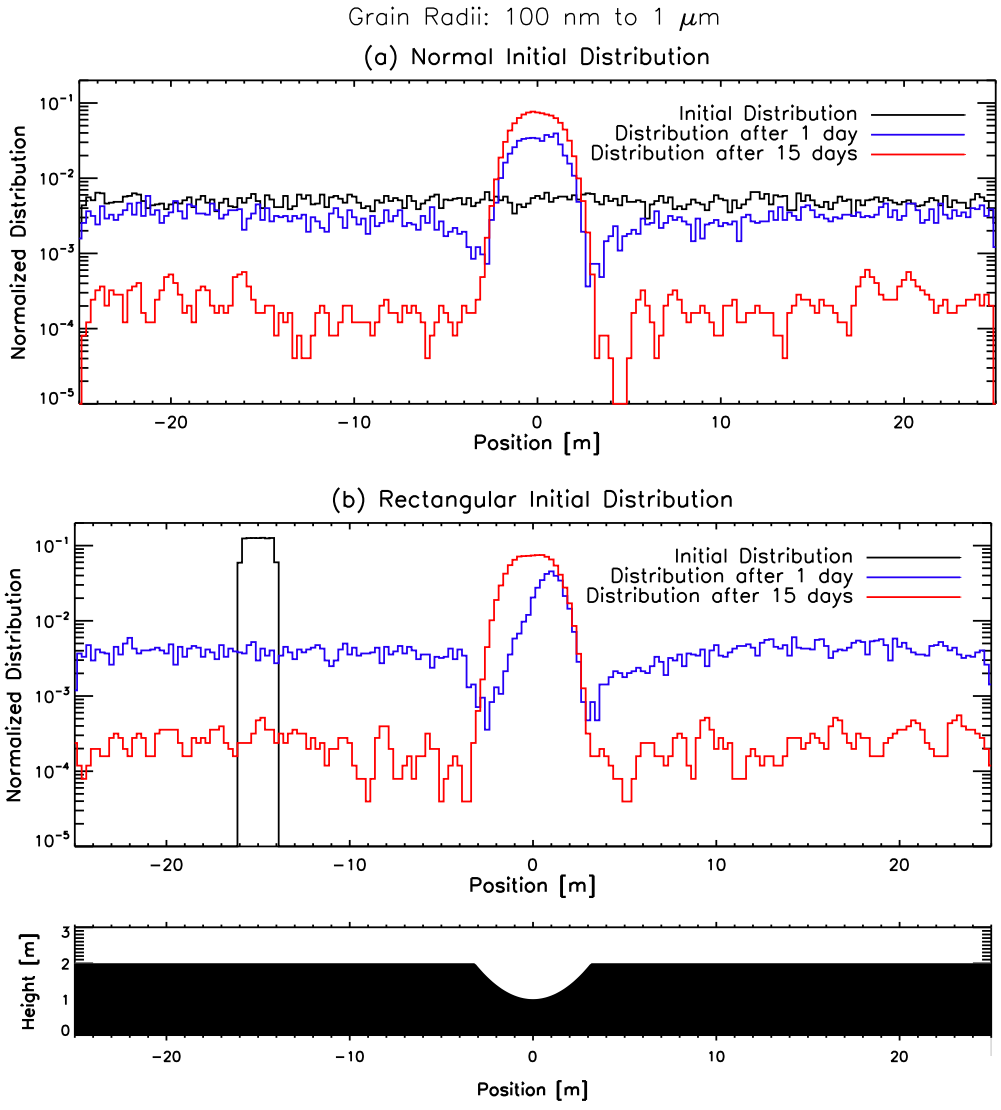

Fig. 7. The spatial distribution of dust grains with radii between 100 nm and 1 μm, shown initially (black), after one lunar day (blue), and after 15 lunar days (red). Panel (a) shows results for a normalized initial distribution, while panel (b) shows results for a rectangular initial distribution two meters wide centered at −15 m. For reference, the crater topography is shown as the lowest panel. (For interpretation of the references to color in this figure legend, the reader is referred to the web version of this article.)

Author's personal copy

grains are periodic, in that if a grain reaches a boundary ($x = \pm 25$ m), it is re-introduced at the opposite boundary with continuous variables. We used periodic boundary conditions to account for grains that are produced beyond the simulation boundary and transported inwards toward the crater. The large separation distance between the main crater and its "neighboring" mirrored crater is great enough that we do not expect any feedback or interference due to the periodic boundary conditions. The distribution of grains on the lunar surface at any given time is continuously tracked, and the probability of launching a grain at a position is given by the instantaneous normalized surface location distribution. When the simulation arrives at dusk, the plasma parameters are set to zero while the transport code continues to run. In effect, all grains follow purely ballistic trajectories throughout the lunar night.

Fig. 7a shows the net dust grain spatial distribution at $t = 0$ (black), $t = 1$ lunar day (blue), and $t = 15$ lunar days (red), as a function of horizontal distance across the lunar surface for grains with radii evenly distributed in size between 100 nm and 1 μm. For reference, the surface topography is shown as a function of horizontal distance at the bottom of Fig. 7. As outlined above, the grains are initially equally distributed in position across the lunar surface; however, by the conclusion of one lunar day, the dust grain spatial distribution has significantly changed, with a slight decrease in density for dust grains farther than 5 m from the crater center (in either direction), a decreasing probability for dust grains within 2–3 m of the crater edge, and a pronounced accumulation of dust grains within the crater itself. By the conclusion of 15 lunar days, the spatial distribution of dust grains outside the crater has dropped an order of magnitude, while the spatial distribution of dust grains within the crater has continued to increase. While we have only shown the spatial distribution at $t = 1$ and 15 lunar days, the net accumulation with the crater reaches an equilibrium within 4–7 lunar days, and thus, the spatial distribution at $t = 15$ lunar days is in equilibrium.

While Fig. 7a has shown that dust grains will accumulate in craters via electrostatic transport, we wish to ensure that such an effect is not dependent on the initial spatial distribution of dust grains. Therefore, Fig. 7b shows the dust grain spatial distributions at $t = 0$, 1, and 15 lunar days for an initial rectangular distribution of dust grains with positions, $-16 < x < -14$. The subsequent distribution at $t = 1$ lunar day is unevenly distributed within the crater, reflecting the asymmetry in the starting distribution. By $t = 15$ lunar days, however, the distribution has reached an equilibrium identical to that in Fig. 7a. This result shows that the method of electrostatically trapping lunar dust grains within craters is not dependent on the initial distribution of available grains.

The electrostatic trapping efficiency of the crater can also be analyzed as a function of grain radius. Fig. 8 shows the equilibrium distribution of dust grains as a function of horizontal position for three ranges of grain sizes: 10–100 nm, 100 nm–1 μm, and 1–10 μm, starting with a normal initial distribution. All distributions were run for 15 days in order to ensure that the distribution reached equilibrium. The two largest size bins show essentially identical results, with a relatively strong trapping efficiency, while the smallest size bin shows relatively weaker trapping. By analyzing groups of individual trajectories, we attribute this effect to the relative strength between electrostatic and gravitational forces for each range of sizes. Smaller grains have a higher charge-to-mass ratio and correspondingly, are typically more dominated by electrostatic forces. A small grain launched from within the crater will be more likely to escape due to the relatively strong impulse it will gain from the near-surface electric fields. The trajectories of larger grains are not significantly modified by the presence of local electric fields due to their low charge-to-mass ratio, and thus, remain more effectively trapped in the crater. This trapping is mainly due to topographic relief, in that the crater walls will tend to trap grains within the crater. We note here that while craters may be more efficient at trapping larger particles, this does not necessarily imply that craters will accumulate larger numbers of greater sized grains. The launching rate as a function of grain size is not well constrained for dust grains on the lunar or asteroidal surfaces, and is perhaps orders of magnitude larger for smaller grains than for larger grains.

As a final investigation into the dust grain trapping efficiency of craters, we repeated the dust transport simulations with two additional initial launch velocities, 0.5 and 2.0 m/s. In order to quantify the amount of trapping, we calculated the net increase in dust grain density within the crater compared to the initial distribution. Fig. 9 shows the net dust grain accumulation within the crater as a

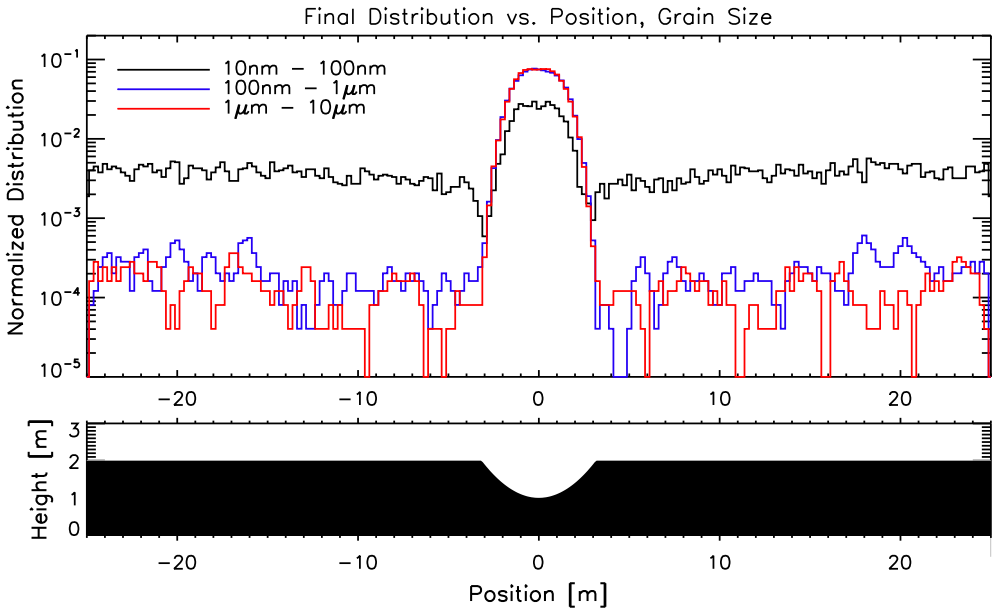

Fig. 8. The final spatial distribution of dust grains for three different size ranges, for a normalized initial distributions and an initial launch velocity of 1.0 m/s. For reference, the crater topography is shown as the lower panel.

Author's personal copy

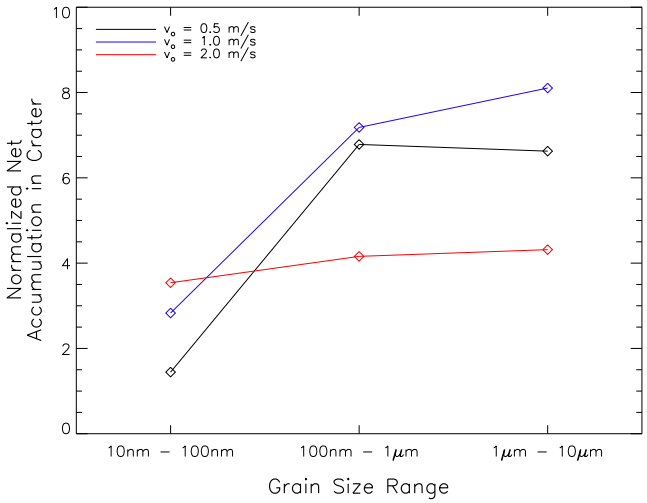

Fig. 9. The normalized net accumulation within the crater for each grain size range, for the three initial velocities tested.

function of grain size for the three initial velocities. For the two slower velocities, the net accumulation reflects the trends presented earlier for the 1.0 m/s initial velocity, in that larger grains tend to accumulate in the crater more easily than their smaller counterparts. For the fastest initial velocity considered of 2.0 m/s, the net accumulation for the two larger size bins (100 nm–1 μm and 1–10 μm) decrease significantly, while the accumulation for the smallest size grains increases modestly. For the larger grains, this is best explained by simple kinematics, in that the higher initial velocities allow the grains to obtain higher maximum heights, leading to easier escape over the crater walls. In contrast, the faster initial velocity causes an increase in net accumulation for the smallest grains, 10–100 nm. This may seem somewhat counterintuitive relative to the explanation for the larger size grains; however, the answer lies in the greater role of electrostatic forces. Previous one-dimensional dust grain tracing simulations have shown that increasing initial launch velocity causes a decrease in dust grain levitation and transport (Poppe and Horányi, 2010). This effect is attributed to the inability of the sheath electric fields to electrostatically reflect charged grains that have relatively large downward velocities. For smaller grains, this effect becomes more pronounced, as the longer charging time of smaller grains (Horányi, 1996) implies that they will not have attained their maximum charge upon re-entering the sheath region. Consequently, the sheath electric force cannot overcome the grain's downward velocity. In sum, as the initial velocity for the smallest grains increases, their ability to be electrostatically levitated, and in turn ejected, from the crater decreases and thus, more 10–100 nm sized grains accumulate within the crater.

4. Discussion and conclusion

We have presented three-dimensional, self-consistent, electrostatic PIC simulations of the lunar photoelectron sheath both above and within an approximately 7 m diameter crater on the day-lit lunar surface. The PIC simulations have accounted for a range of phenomena present in the lunar environment, including photoemission from the lunar surface from illumination by solar UV radiation, the inflowing supersonic solar wind, a meter-scale crater on the lunar surface, and the shadowing effects to which these craters give rise. At locations relatively far from the presence of the crater, we found photoelectron sheath potentials and electric fields typical of that from previous estimations, simulations, and observations (Freeman and Ibrahim, 1975; Halekas et al., 2008; Poppe and Horányi, 2010). Interestingly, these simulations do not show the presence of a non-monotonic potential layer above the surface of the Moon while in the solar wind, as previous simulations and observations have indicated (Poppe and Horányi, 2010; Poppe et al., 2011, 2012; Halekas et al., 2012). We attribute this to the simulation volume to which our computational constraints limit us. The maximum simulation height we have presented here is 15 m. Comparison with previous simulations of non-monotonic potentials (Poppe and Horányi, 2010, Fig. 3a) shows that this height is insufficient to allow the incident solar wind to develop the initially decreasing potential required for a non-monotonic potential. Future work will address the effect that non-monotonic potentials may have on the plasma environment above day-lit craters either via two-dimensional PIC simulations (allowing a greater simulation height) or via greater computational resources.

While we have presented simulation results for a single crater geometry, we can also make a qualitative assessment on how our results would change in the presence of a shallower or steeper crater. In the shallower case, the range of angles between the surface normal and the incident solar UV radiation and solar wind will be smaller, resulting in less variation in photoemission and surface charging. Consequently, we would expect the electrostatic potential above such a crater to have less spatial variation. In turn, this would imply weaker electric fields near the edges and rims of the crater. Shallower craters will also have fewer conditions under which regions inside the crater are shadowed by the crater rim and therefore, fewer regions of negatively charged surface. In the case of a steeper crater, we may expect the opposite effect, in that variation in the incident illumination angle will increase and induce greater variability in photoemission from the crater surface. For craters that are too steep, however, a greater percentage of the surface will be shadowed through the lunar day, decreasing the overall strength of the photoelectron sheath within the crater. Future work with the VORPAL PIC code can explore the variation in the photoelectron sheath induced by changes in the crater dimensions.

An additional conclusion that can be drawn from our simulation regards the formation of anomalously large electric fields (>10^5 V/m) near the lunar terminator (De and Criswell, 1977; Criswell et al., 1977), known as 'supercharging'. Lunar surface supercharging was predicted to occur near the lunar terminator as sunlit and shadowed regions in close proximity accumulate significant amounts of differential charge separation over short spatial scales. While we have not conducted an exhaustive series of simulations of all manner of shadowing morphology, our simulations do not contain fields much larger than 10 V/m, much lower than that predicted for supercharging. The explanation for the lack of such an effect lies in the ability of both the solar wind electrons, a thermalized, 10 eV population, and any photoelectrons near the surface to efficiently short out electric fields on the scale of the near-surface Debye length (≈1–10 m). Indeed, previous analytical models of the near-surface electric field environment near the lunar terminator have predicted electric fields no greater than 3 V/m, albeit without topography (Farrell et al., 2007); however, the authors do suggest that orographic effects from the presence of lunar crater rims may give rise to enhanced electric fields. For the crater scale and geometry modeled here, we do predict electric fields enhanced near crater rims relative to the electric field strength far from the crater; however, the overall magnitude of such electric fields does not rise much above 10 V/m. Recent two-dimensional PIC simulations have simulated orographic effects from lunar craters on the scale of approximately 1 km and found the presence of wake-like structures in the plasma environment; however, these simulations as well have predicted maximum electric field strengths only on the order of 1 V/m (Zimmerman et al., 2011). It is possible that there exists a range

Author's personal copy

of scale lengths between 10 m and 1 km where topography and associated orographic effects may give rise to electric fields greater than that found in these and previous simulations, and future work should investigate this possibility. Additionally, recent experimental measurements of the electric potential and electric field in a laboratory-generated photoelectron sheath could be extended to investigate and confirm the presence of complex electric fields as a result of surface topography (Dove et al., 2012).

By using the plasma environment results from the PIC model, we have simulated the electrostatic charging, levitation and transport of dust grains ranging from 10 nm to 10 μm in radius. By analyzing the bulk trajectories of approximately 25,000 dust grains, we have drawn several conclusions, including,

- Electrostatically transported dust grains will tend to accumulate within crater boundaries as a result of the presence of complex electric fields near the crater edges.
- Dust grains trapped within craters form equilibrium spatial distributions centered within the crater.
- The initial distribution of dust grains on the lunar surface does not impact the eventual equilibrium distribution of grains in the crater.
- The crater traps larger grains at a higher efficiency than for smaller grains due to the varying relative importance of the electrostatic and gravitational forces as a function of grain size.
- The initial launch velocity of dust grains off of the lunar surface can significantly affect the trapping efficiency of craters.

As a whole, these results confirm earlier models of electrostatic dust transport near lunar and/or asteroidal craters (Colwell et al., 2005; Hughes et al., 2008), while extending our understanding of how surface relief, via the presence of complex electrostatic fields, affects both the individual and bulk transport of dust grains.

We do find, however, that the significant lack of knowledge about the dust grain launching mechanism, including the launching probability as a function of grain size and plasma conditions, and the distribution of initial velocities prevents us from establishing absolute rates on dust transport into craters. Recent work has shown that for the smallest grain sizes considered in our model (<5 μm), cohesion between grains will dominate over both electrostatic and gravitational forces (Scheeres et al., 2010; Hartzell and Scheeres, 2011), implying that spontaneous electrostatically-induced ejection of micron-sized dust grains is unlikely. Micrometeoroid bombardment of the lunar surface does provide a mechanism to eject particles with a range of sizes and initial charges off of airless surfaces. The ejection velocity distribution from micrometeoroid bombardment is typically assumed to be a power law governed by a slope and minimum velocity (Krivov et al., 2003, and references therein), with both parameters depending on the surface (target) properties, the impact velocity, the energy partitioning between the impactor and the ejecta, and the total yield (Krüger et al., 2000). For certain sets of these values, minimum ejecta velocities can range down to less than 1 m/s, which would potentially provide a source of low-speed dust grains; however, we must caution that the parameters of ejecta production at the Moon or other airless bodies are somewhat uncertain. Additionally, we must point out that previous work has analyzed micrometeoroid bombardment as a potential source of micron-sized, electrostatically levitated dust grains at the Asteroid 433 Eros and found it insufficient in magnitude to explain the observed dust ponds (Colwell et al., 2005). A full understanding of the mechanics and subsequent dynamics of dust grains in electrostatically complex environments such as the surface of the Moon requires in situ measurements in order to constrain the size, velocity, and charge of electrostatically transported grains (Wang et al., 2008; Duncan et al., 2011).

We identify a number of investigations as future work, including the role that the crater size (with respect to the local Debye length) and the lunar latitude of the crater play in modifying the plasma environment and dust transport. For example, we expect that craters on the order of or smaller than the photoelectric Debye length of approximately 1 m will not significantly alter the plasma environment, as any local loss of quasineutrality (and associated electric fields) will be shorted out by the photoelectrons. Also, craters at significant lunar latitudes, where one side of the crater may experience continuously less solar UV radiation and solar wind flux may accumulate dust grains asymmetrically due to a persistent, asymmetric plasma environment. Finally, the presence of boulders near or within the crater should be studied, as these objects will tend to break the symmetry of the crater and may introduce complex patterns in both the plasma environment and electrostatic dust transport. Many of the geometries that could be simulated with lunar topography may also apply to the construction and emplacement of man-made structures. A full understanding of the plasma and electric field environment near such structures is critical for successfully operating and living with the lunar environment. Further laboratory and in situ investigations are also required to understand electrostatic launching and transport of lunar and asteroidal dust grains.

Acknowledgments

The authors thank the NASA Lunar Science Institute for their support through the Colorado Center for Lunar Dust and Atmospheric Studies, Grant #NNX08AY77G. A.R.P. gratefully acknowledges support from a NASA Earth and Space Science Graduate Fellowship, Grant #NNX08BA17H, and from the NASA Lunar Science Institute through the Dynamic Response of the Environment at the Moon (DREAM) team. The authors also thank P. Messmer for useful discussions in designing the simulation model and two anonymous reviewers from helpful and constructive comments.

References

Berg, O.E., Richardson, F.F., Burton, H., 1973. Apollo 17 preliminary science report. Tech. Rep. NASA SP-330, National Aeronautics and Space Administration. pp. 16–21.

Berg, O.E., Richardson, F.F., Rhee, J.W., Auer, S., 1974. Preliminary results of a cosmic dust experiment on the Moon. Geophys. Res. Lett. 1 (7), 289–290.

Borisov, N., Mall, U., 2006. Charging and motion of dust grains near the terminator of the Moon. Planet. Space Sci. 54, 572–580.

Cheng, A.F., Izenberg, N., Chapman, C.R., Zuber, M.T., 2002. Ponded deposits on Asteroid 433 Eros. Meteorit. Planet. Sci. 37, 1095–1105.

Colwell, J.E., Gulbis, A.A.S., Horányi, M., Robertson, S., 2005. Dust transport in photoelectron layers and the formation of dust ponds on Eros. Icarus 175, 159–169.

Criswell, D.R., 1972. Lunar dust motion. Proc. Lunar Sci. Conf. 3, 2671–2680.

Criswell, D.R., De, B.R., 1977. Intense localized photoelectric charging in the lunar sunset terminator region: 2. Supercharging at the progression of sunset. J. Geophys. Res. 82 (7), 1005–1007.

De, B.R., Criswell, D.R., 1977. Intense localized photoelectric charging in the lunar sunset terminator region: 1. Development of potentials and fields. J. Geophys. Res. 82 (7).

Dove, A., Horányi, M., Wang, X., Piquette, M., Poppe, A.R., Robertson, S., 2012. Experimental study of a photoelectron sheath. Phys. Plasmas 19 (043502).

Duncan, N. et al., 2011. The Electrostatic Lunar Dust Analyzer (ELDA) for the detection and trajectory measurements of slow-moving dust particles on the lunar surface. Planet. Space Sci. 59, 1446–1454.

Farrell, W.M., Stubbs, T.J., Vondrak, R.R., Delory, G.T., Halekas, J.S., 2007. Complex electric fields near the lunar terminator: The near-surface wake and accelerated dust. Geophys. Res. Lett. 34, 1–5.

Farrell, W.M. et al., 2008. Loss of solar wind plasma neutrality and affect on surface potentials near the lunar terminator and shadowed polar regions. Geophys. Res. Lett. 35, 1–5.

Farrell, W.M. et al., 2010. Anticipated electrical environment within permanently shadowed lunar craters. J. Geophys. Res. 115, E03004, 1–14.

Author's personal copy

Feuerbacher, B., Anderegg, M., Fitton, B., Laude, L.D., Willis, R.F., Grard, R.J.L., 1972. Photoemission from lunar surface fines and the lunar photoelectron sheath. Proc. Lunar Sci. Conf. 3, 2655–2663.
Flanagan, T.M., Goree, J., 2006. Dust release from surfaces exposed to plasma. Phys. Plasmas 13, 1–11.
Freeman, J.W., Ibrahim, M., 1975. Lunar electric fields, surface potential and associated plasma sheaths. The Moon 14, 103–114.
Fu, J.H.M., 1971. Surface potential of a photoemitting plate. J. Geophys. Res. 76 (10), 2506–2509.
Glenar, D.A., Stubbs, T.J., McCoy, J.E., Vondrak, R.R., 2011. A reanalysis of the Apollo light scattering observations, and implications for lunar exospheric dust. Planet. Space Sci. 59, 1695–1707.
Guernsey, R.L., Fu, J.H.M., 1970. Potential distribution surrounding a photo-emitting plate in a dilute plasma. J. Geophys. Res. 75 (16), 3193–3199.
Halekas, J.S., Delory, G.T., Lin, R.P., Stubbs, T.J., Farrell, W.M., 2008. Lunar Prospector observations of the electrostatic potential of the lunar surface and its response to incident currents. J. Geophys. Res. 113, A09102, 1–16.
Halekas, J.S., Poppe, A., Delory, G.T., Farrell, W.M., Horányi, M., 2012. Solar wind electron interaction with the dayside lunar surface and crustal magnetic fields: Evidence for precursor effects. Earth Planets Space 64, 73–82.
Hartzell, C.M., Scheeres, D.J., 2011. The role of cohesive forces in particle launching on the Moon and asteroids. Planet. Space Sci. 59 (14), 1758–1768.
Heroux, M.A. et al., 2005. An overview of the Trilinos Project. ACM Trans. Math. Software 31 (3), 397–423.
Horányi, M., 1996. Charged dust dynamics in the Solar System. Annu. Rev. Astron. Astrophys. 34, 383–418.
Hughes, A.L.H., Colwell, J.E., DeWolfe, A.W., 2008. Electrostatic dust transport on Eros: 3-D simulations of pond formation. Icarus 195, 630–648.
Ip, W.-H., 1986. Electrostatic charging and dust transport at Mercury's surface. Geophys. Res. Lett. 13 (11), 1133–1136.
Krivov, A.V., Sremčevič, M., Spahn, F., Dikarev, V.V., Kholshevnikov, K.V., 2003. Impact-generated dust clouds around planetary satellites: Spherically symmetric case. Planet. Space Sci. 51, 251–269.
Krüger, H., Krivov, A.V., Grün, E., 2000. A dust cloud of ganymede maintained by hypervelocity impacts of interplanetary micrometeoroids. Planet. Space Sci. 48 (5), 1457–1471.
Lee, P., 1996. Dust levitation on asteroids. Icarus 124, 181–194.
McCoy, J.E., Criswell, D.R., 1974. Evidence for a high altitude distribution of lunar dust. Proc. Lunar Sci. Conf. 5, 2991–3005.
Nieter, C., Cary, J.R., 2004. VORPAL: A versatile plasma simulation code. J. Comp. Phys. 196, 448–473.
Nitter, T., Havnes, O., Melandsø, F., 1998. Levitation and dynamics of charged dust in the photoelectron sheath above surfaces in space. J. Geophys. Res. 103 (A4), 6605–6620.
Olhoeft, G.R., Frisillo, A.L., Strangway, D.W., 1974. Electrical properties of lunar soil sample 15301,38. J. Geophys. Res. 79 (11), 1599–1604.
Pelizzari, M.A., Criswell, D.R., 1978. Lunar dust transport by photoelectric charging at sunset. Proc. Lunar Sci. Conf. 9, 3225–3237.
Poppe, A.R. et al., 2012. A comparison of ARTEMIS observations and particle-in-cell modeling of the lunar photoelectron sheath in the terrestrial magnetotail. Geophys. Res. Lett. 39, L01102, 1–6.
Poppe, A., Horányi, M., 2010. Simulations of the photoelectron sheath and dust levitation on the lunar surface. J. Geophys. Res. 115, A08106, 1–9.
Poppe, A., Halekas, J.S., Horányi, M., 2011. Negative potentials above the day-side lunar surface in the terrestrial plasma sheet: Evidence of non-monotonic potentials. Geophys. Res. Lett. 38, L02103, 1–5.
Rennilson, J.J., Criswell, D.R., 1974. Surveyor observations of lunar horizon-glow. The Moon 10, 121–142.
Robertson, S., Gulbis, A.A.S., Colwell, J., Horányi, M., 2003. Dust grain charging and levitation in a weakly collisional plasma sheath. Phys. Plasmas 10, 3874–3880.
Robinson, M.S., Thomas, P.C., Veverka, J., Murchie, S., Carcich, B., 2001. The nature of ponded deposits on Eros. Nature 413, 396–400.
Scheeres, D.J., Hartzell, C.M., Sánchez, P., Swift, M., 2010. Scaling forces to asteroid surfaces: The role of cohesion. Icarus 210, 968–984.
Sickafoose, A.A., Colwell, J.E., Horányi, M., Robertson, S., 2000. Photoelectric charging of dust particles in vacuum. Phys. Rev. Lett. 84 (26), 6034–6037.
Sickafoose, A.A., Colwell, J.E., Horányi, M., Robertson, S., 2001. Experimental investigations of photoelectric and triboelectric charging of dust. J. Geophys. Res. 106 (A5), 8343–8356.
Sickafoose, A.A., Colwell, J.E., Horányi, M., Robertson, S., 2002. Experimental levitation of dust grains in a plasma sheath. J. Geophys. Res. 107 (A11), 1–11.
Stubbs, T.J., Vondrak, R.R., Farrell, W.M., 2007. Impact of dust on lunar exploration. In: Proc. 'Dust in Planetary Systems', Kauai, Hawaii, USA, 239–243.
Veverka, J. et al., 2001. Imaging of small-scale features on 433 Eros from NEAR: Evidence for a complex regolith. Science 292 (484), 484–488.
Wang, X., Horányi, M., Sternovsky, Z., Robertson, S., Morfill, G.E., 2007. A laboratory model of the lunar surface potential near boundaries between sunlit and shadowed regions. Geophys. Res. Lett. 34, L16104, 1–5.
Wang, X., Horányi, M., Robertson, S., 2008. Plasma probes for the lunar surface. J. Geophys. Res. 113, A08108, 1–5.
Wang, X., Horányi, M., Robertson, S., 2009. Experiments on dust transport in plasma to investigate the origin of the lunar horizon glow. J. Geophys. Res. 114, 1–6.
Wang, X., Horányi, M., Robertson, S., 2010. Investigation of dust transport on the lunar surface in a laboratory plasma with an electron beam. J. Geophys. Res. 115, A11102, 1–6.
Wang, X., Horányi, M., Robertson, S., 2011. Dust transport near electron beam impact and shadow boundaries. Planet. Space Sci. 59, 1791–1794.
Zimmerman, M.I., Farrell, W.M., Stubbs, T.J., Halekas, J.S., Jackson, T.L., 2011. Solar wind access to lunar polar craters: Feedback between surface charging and plasma expansion. Geophys. Res. Lett. 38, L19202, 1–5.